

Joint 3D modelling of the polarized Galactic synchrotron and thermal dust foreground diffuse emission

L. Fauvet¹, J. F. Macías-Pérez¹, J. Aumont^{2,3}, F.X. Désert^{1,4,5}, T.R. Jaffe^{3,6},
A.J. Banday³, M. Tristram⁷, A.H. Waelkens⁸, and D. Santos¹

¹ LPSC, Université Joseph Fourier Grenoble 1, CNRS/IN2P3, Institut National Polytechnique de Grenoble, 53 avenue des Martyrs, 38026 Grenoble cedex, France

² Institut d'Astrophysique Spatiale, Centre Universitaire d'Orsay, Bat. 121, 91405 Orsay Cedex, France

³ Centre d'Etude Spatiale des Rayonnements, 9 avenue du Colonel Roche, 31028 Toulouse, France

⁴ Laboratoire d'astrophysique de Grenoble, OSUG, Université Joseph Fourier BP 53, 38041 Grenoble CEDEX 9, France

⁵ Institut Neel, 25 rue des Martyrs, BP 166, 38042 Grenoble cedex 9, France

⁶ Jodrell Bank Centre for Astrophysics, School of Physics and Astronomy, The University of Manchester, Oxford Road, Manchester M13 9PL, UK

⁷ Laboratoire de l'Accélérateur Linéaire, BP 34, 91898 Orsay Cedex France

⁸ Max-Planck Institute for Astrophysics, Karl Schwarzschild Str. 1, 85741 Garching, Germany

October 25, 2018

ABSTRACT

Aims. We present for the first time a coherent model of the polarized Galactic synchrotron and thermal dust emissions which are the main diffuse foreground for the measurement of the polarized power spectra of the CMB fluctuations with the Planck satellite mission.

Methods. We produce 3D models of the Galactic magnetic field including regular and turbulent components, and of the distribution of matter in the Galaxy, relativistic electrons and dust grains. By integrating along the line of sight we construct maps of the polarized Galactic synchrotron and thermal dust emission for each of these models and compare them to currently available data. We consider the 408 MHz all-sky continuum survey, the 23 GHz band of the Wilkinson Microwave Anisotropy Probe and the 353 GHz Archeops data.

Results. The best-fit parameters obtained are consistent with previous estimates in the literature based only on synchrotron emission and pulsar rotation measurements. They allow us to reproduce the large scale structures observed on the data. Poorly understood local Galactic

structures and turbulence make difficult an accurate reconstruction of the observations in the Galactic plane.

Conclusions. Finally, using the best-fit model we are able to estimate the expected polarized foreground contamination at the Planck frequency bands. For the CMB bands, 70, 100, 143 and 217 GHz, at high Galactic latitudes although the CMB signal dominates in general, a significant foreground contribution is expected at large angular scales. In particular, this contribution will dominate the CMB signal for the B modes expected from realistic models of a background of primordial gravitational waves.

Key words. ISM: general – Methods: data analysis – Cosmology: observations – Submillimeter

1. Introduction

The PLANCK satellite mission, currently in flight, should permit the more accurate measurements of the CMB anisotropies both in temperature and polarization. Planck, which observes the sky on a wide range of frequency bands from 30 to 857 GHz, has a combined sensitivity of $\frac{\Delta T}{T_{CMB}} \sim 2 \frac{\mu K}{K}$ and an angular resolution from 33 to 5 arcmin (PLANCK bluebook 2004). Of particular interest is the measurement of the polarization B modes which implies the presence of tensor fluctuations from primordial gravitational waves generated during inflation. Planck should be able to measure the tensor-to-scalar ratio, r , down to 0.1 (Betoule et al 2009, Efstathiou et al 2009) in the case of a nominal mission (2 full-sky surveys) and to 0.05 for the Extended Planck Mission: four full-sky surveys (Efstathiou & Gratton 2009). The value of r sets the energy scale of the inflation (Peiris et al 2003) and then provides constraints on inflationary models (Baumann et al 2009).

To achieve this high level of sensitivity it is necessary to accurately estimate the temperature and polarization foregrounds mainly from diffuse Galactic emission components – synchrotron, thermal and rotational dust, and free-free – as well as from the Galactic and extra-Galactic point-like and compact sources. Indeed, at the Planck frequency bands these foreground components may dominate the CMB signal and therefore, they need to be either masked or subtracted prior to any CMB analysis. For this purpose, the Planck collaboration plans to use component separation techniques (see Leach et al 2008 for a summary) in addition to the traditional masking of highly contaminated sky regions including identified point-like and compact sources. As these component separation techniques will be mainly based on Planck data only, one of the main issues will be to estimate the residual foreground contamination on the final CMB temperature and polarization maps. These residuals will translate into systematic biases and larger error bars on the estimation of the temperature and polarization power spectra of the CMB fluctuations (see Betoule et al 2009 for a recent study). Thus, they

will impact the precision to which cosmological information can be retrieved from the Planck data.

For polarization the main foreground contributions will come from the diffuse Galactic synchrotron and thermal dust emission. From the WMAP observations, Page et al 2007 have shown that the radio synchrotron emission from relativistic electrons is highly polarized, up to 70 %, between 23 and 94GHz. Furthermore, Benoît et al 2004, Ponthieu et al 2005 have observed significantly polarized thermal dust emission, up to 15 % at the 353 GHz Archeops channel. By contrast the diffuse free-free emission is not polarized and the anomalous microwave emission has been measured to be weakly polarized, $3_{-1.9}^{+1.3}$ %, (Battistelli et al 2006). Finally, at the Planck frequency bands the polarized contribution from compact and point sources is expected to be weak for radio (Nolta et al 2009) and dust (Desert et al 2008) sources. The spatial and frequency distribution of both Galactic synchrotron and thermal dust polarized emission at the Planck frequencies are not well known and the only available information comes from microwave and submillimetre observations. For synchrotron, Faraday rotation (Burn et al 1966) makes it very difficult to extrapolate the polarized observed radio emission (Wolleben et al 2006, Wolleben et al 2007, Carretti et al 2009) to the microwave domain. For thermal dust, polarized observations are not currently available in the infrared and the current optical data (Heiles 2000) are too sparse (Page et al 2007) for a reliable extrapolation to lower frequencies.

The diffuse Galactic synchrotron emission is produced by relativistic electrons spiraling around the Galactic magnetic field lines and its polarization is orthogonal both to the line-of-sight and to the field direction (Ribicki & Lightman 1979). Based on these statements, Page et al 2007 proposed to model the polarized synchrotron Galactic emission observed by the WMAP satellite using a 3D model of the Galaxy including the distribution of relativistic electrons and the Galactic magnetic field structure. Although this model allowed them to explain the observed polarization angle at the 23 GHz band where the synchrotron emission dominates, it was not used for the CMB analysis. Instead they constructed a template of the polarized synchrotron emission from the 23 GHz band and extrapolated it to higher frequencies. Independently, Han et al 2004, Han et al 2006 has also proposed a 3D model of the Galactic free electrons (Cordes & Lazio 2002) and of the Galactic magnetic field including a regular and a turbulent component to explain the observed rotation measurements on known pulsars. Based on previous works Sun et al 2008 has performed a combined analysis of the polarized WMAP data and of the rotation measurements of pulsars using the publicly available HAMMURABI code (Waelkens et al 2009) for computing the integrated emission along th line-of-sight.

This work has been extended by Jaffe et al 2009 for the study of the Galactic plane using a MCMC algorithm for the determination of the parameter of the models and by Jansson et al 2009 for the full sky using a likelihood analysis for parameter estimation.

Dust grains in the Interstellar Medium (ISM) are heated by stellar radiation and radiate in the form of thermal dust emission (Desert et al 1998). They are considered to be oblate and to align with their longitudinal axis perpendicular to the magnetic field lines (Davis & Greenstein 1951). When aligned they will end up rotating with their angular moment parallel to the magnetic field direction. As the thermal dust emission is more efficient along the long axis, this generates linear polarization orthogonal to the magnetic field direction and to the line-of-sight. The polarization fraction of the emission depends on the distribution of the size of the grains and is about a few percent at the millimeter wavelengths (Hildebrand et al 1999, Vaillancourt 2002). Ponthieu et al 2005 concluded that the polarized emission observed in the 353 GHz Archeops data was associated with the thermal dust emission and proposed a simple magnetic field pattern to explain the measured direction of polarization on the Galactic plane. Page et al 2007 suggested that part of the observed polarized emission at the 94 GHz WMAP data was also due to thermal dust. They modeled it using the observed polarization direction of stellar light (Heiles 2000) which from the above statement must be perpendicular to that of thermal dust.

With the prospect of the data analysis of the Planck satellite mission in mind, we present here consistent physical models of the synchrotron and thermal dust emission based on the 3D distribution of relativistic electrons and dust grains on the Galaxy, and on the 3D pattern of the Galactic magnetic field. The paper is structured as follows: Sect. 2 describes the 408 MHz all-sky continuum survey (Haslam et al 1982), the five-year WMAP data set (Page et al 2007) and the Archeops data (Ponthieu et al 2005) used in the analysis. In Sect.3 we describe in detail the models. Section 4 describes the statistical comparison of data and models. In Sect. 5 we discuss the impact of polarized foreground emission on the measurement of the polarized CMB emission with the Planck satellite. Finally, conclusions are presented in Section 6.

2. Observational data

2.1. Diffuse Galactic synchrotron emission

The Galactic diffuse synchrotron emission is important at radio and microwave observation frequencies. Although its SED is not accurately known it can be well represented by a power law in antenna temperature $I_\nu \propto \nu_s^\beta$ with the synchrotron spectral index ranging from -2.7 to -3.3 (Kogut et al 2007, Gold et al 2009). Radio frequency surveys as the

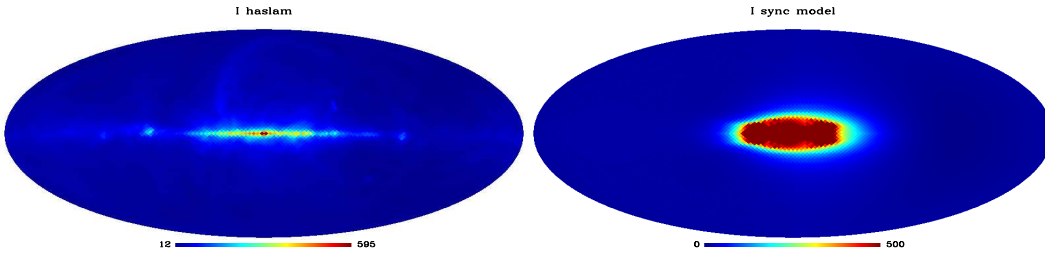


Fig. 1. Intensity maps at 408 MHz in K_{RJ} units for the Haslam data (*left*) and built with the mode of synchrotron emission with MLS magnetic field for the best fit model parameters (*right*).

Leider 408 MHz and 1.4 GHz surveys (Brouw & Spoelstra 1976, Wolleben et al 2006), the Parkes survey at 2.4 GHz (Duncan 1999), and the MGLS survey (*Medium Galactic Latitude Survey*) at 1.4 GHz (Uyaniker et al 1999) are generally used to trace the Galactic diffuse synchrotron emission in intensity. For polarization Faraday rotation makes things more complex as for frequencies lower than 10 GHz strong depolarization is expected (Burn et al 1966, Sun et al 2008, Jaffe et al 2009, Jansson et al 2009) so that the best Galactic diffuse synchrotron tracers are at high frequency like the WMAP survey at 23 GHz (Page et al 2007).

2.1.1. 408 MHz all-sky continuum survey

In the following we use the 408 MHz all-sky continuum survey (Haslam et al 1982), after subtraction of the free-free emission at this frequency, as a tracer of the Galactic synchrotron emission in temperature. We use the HEALpix (Górski et al 2005) format map available on the LAMBDA website¹. The calibration scale of this survey is claimed to be accurate to better than 10 % and the average zero level has an uncertainty of ± 3 K as explained in Haslam et al 1982. To subtract the free-free emission at 408 MHz we use the five-year public WMAP (*Wilkinson Microwave Anisotropies Probe*) free-free foreground map at 23 GHz generated from the maximum entropy method (MEM) described in Hinshaw et al 2007. We have found that the free-free correction has no impact on the final results presented on this paper. We start from the full-sky HEALpix maps at $N_{side} = 512$ (pixel size of 6.9 arcmin) and downgrade them to $N_{side} = 32$ (pixel size of 27.5 arcmin). We then subtract from the Haslam data the free-free component extrapolated from the K-band assuming a power-law dependence of $\nu^{-2.1}$ as in Dickinson et al 2003. The left panel of Figure 1 shows the free-free corrected 408 MHz all-sky survey where we clearly observe the Galactic plane and the North Celestial Spur at high Galactic latitude.

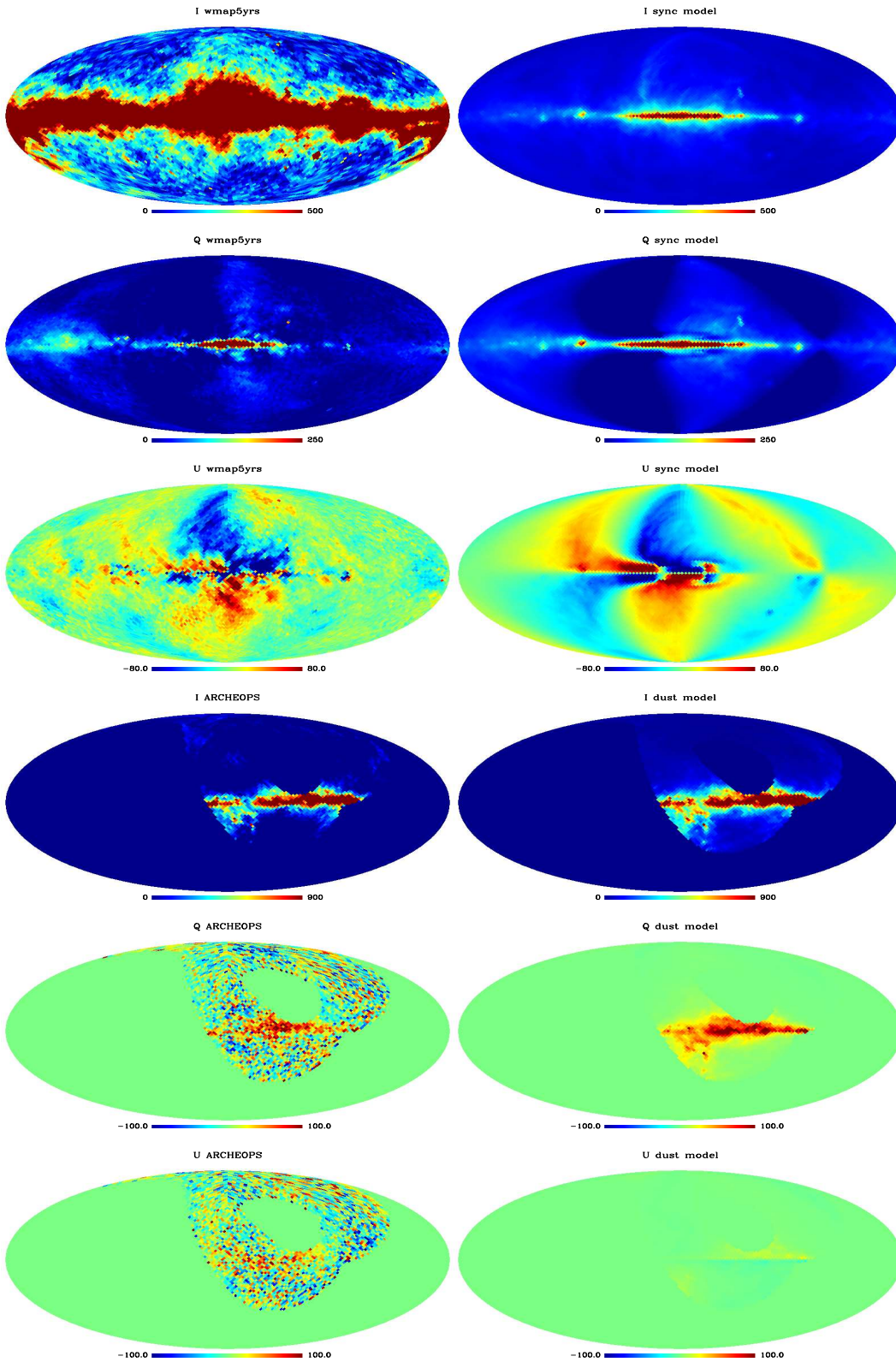


Fig. 2. Form top to bottom: Maps in intensity, I, and polarization Q and U at 23 GHz for the WMAP 5-year data (*left*) and the model of synchrotron emission with MLS magnetic field for the best fit model parameters (*right*) and at 353 GHz for the Archeops data (*left*) and the model of thermal dust emission with MLS magnetic field for the best fit model parameters (*right*). The 353 GHz maps are rotated by 180° for better visualization. All the maps are in K_{RJ} units.

2.1.2. Five-year WMAP polarized data at 23 GHz

To trace the polarized synchrotron emission we use the all-sky five-year WMAP Q and U maps at 23 GHz available on the LAMBDA website in the HEALPix pixelisation scheme (Górski et al 2005). In particular the coadded maps at $N_{side} = 512$ for the K-band (Page et al 2003, Gold et al 2009). These maps are then downgraded to $N_{side} = 32$ to increase the signal-to-noise ratio as we are only interested on very large angular scales and the analysis will be performed on Galactic latitude profiles. The pixel window function will be accounted for in the following. We assume anisotropic white noise on the maps and compute the variance per pixel using the variance per hit provided on the LAMBDA website and the maps of number of hits. The large angular scale correlations on the noise are neglected. We think this has no impact on the final results as very similar results have been obtained using a pixel-to-pixel analysis at $N_{side} = 16$ using the noise correlation matrix. The second and third plots on the left column of Figure 2 show the 23 GHz Q and U maps. We can clearly observe the Galactic plane but also large-scale high Galactic structures.

2.2. Thermal dust

The dust thermal emission in temperature is well traced by the IRAS (Schlegel et al 1998) all-sky observations in the infrared, the FIRAS-COBE (Boulanger et al 1996) all-sky observations in the radio and millimeter domain and the ARCHEOPS (Macías-Pérez et al 2007, Benoît et al 2004) data in the millimeter domain over 30 % of the sky . In polarization early observations by Hiltner 1949, Hall 1949 and later by Heiles 2000 have proved that the starlight emission in the optical domain was polarized and therefore we will expect the thermal dust emission at millimetric wavelength also to be polarized. This was confirmed by the Archeops observations at 353 GHz (Ponthieu et al 2005) that yielded a polarization fraction of about 10 % in the Galactic plane.

Here we use the Archeops 353 GHz Q and U maps as tracers of the polarized thermal dust emission. As shown in the fifth and sixth plots of the left column of Figure 2 they cover about 30 % of the sky with 13 arcmin resolution. In contrast to the WMAP data at 23 GHz, most the signal in the Q and U 353 GHz maps is concentrated on the Galactic plane. These maps are then downgraded to $N_{side} = 32$ to increase the signal-to-noise ratio. As for the WMAP 23 GHz data the noise assumed to be anisotropic white noise on the maps and compute the variance per pixel using the variance provided by the Archeops collaboration (Macías-Pérez et al 2007).

¹ <http://lambda.gsfc.nasa.gov/>

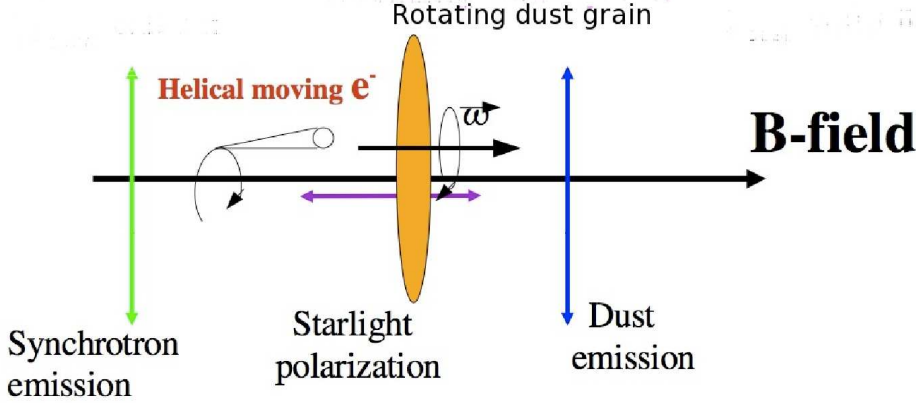


Fig. 3. Schematic view of the direction of polarization of the Galactic synchrotron and dust thermal emission as a function of the Galactic magnetic field direction.

3. 3D modeling of the galaxy

We present in this section a realistic model of the diffuse synchrotron and dust polarized emission using a 3D model of the Galactic magnetic field and of the matter density in the Galaxy. We will consider the distribution of relativistic cosmic-ray electrons (CREs), n_{CRE} , for the synchrotron emission and the distribution of dust grains, n_{dust} , for the dust thermal emission. The total polarized foreground emission observed at a given position on the sky \mathbf{n} and at a frequency ν can be computed by integrating along the line of sight as follows.

Synchrotron

For the synchrotron emission (Ribicki & Lightman 1979) and defining

$$dI_{\nu}^{\text{sync}} = \epsilon^{\text{sync}}(\nu) n_{\text{CRE}}(\mathbf{n}, z) \cdot (B_l(\mathbf{n}, z)^2 + B_t(\mathbf{n}, z)^2)^{(s+1)/4} dz \quad (1)$$

we obtain

$$I_{\nu}^{\text{sync}}(\mathbf{n}) = \int dI_{\nu}^{\text{sync}}, \quad (2)$$

$$Q_{\nu}^{\text{sync}}(\mathbf{n}) = \int dI_{\nu}^{\text{sync}} \cos(2\gamma(\mathbf{n}, z)) p^{\text{sync}}, \quad (3)$$

$$U_{\nu}^{\text{sync}}(\mathbf{n}) = \int dI_{\nu}^{\text{sync}} \sin(2\gamma(\mathbf{n}, z)) p^{\text{sync}}. \quad (4)$$

where I, Q and U are the Stokes parameters and $\epsilon^{\text{sync}}(\nu)$ is an emissivity term. γ is the polarization angle and B_n , B_l and B_t are the magnetic field components along, longitudinal and transverse to the line of sight, \mathbf{n} , and z is a 1D coordinate along the

line-of-sight. s is the exponent of the power-law representing the energy distribution of relativistic electrons in the Galaxy. The polarization fraction, p^{sync} , is related to s , as follows

$$p^{sync} = \frac{s+1}{s+7/3} \quad (5)$$

In the following we will assume a constant value of 3 for s so that the synchrotron emission will be proportional to the square of the perpendicular component of the Galactic magnetic field to the line of sight and $p_{sync} = 0.75$ (Ribicki & Lightman 1979).

Locally, the direction of polarization will be orthogonal to the magnetic field lines and to the line of sight. Then, the polarization angle γ is given by

$$\gamma(\mathbf{n}, s) = \frac{1}{2} \arctan \left(\frac{2B_l(\mathbf{n}, z) \cdot B_t(\mathbf{n}, z)}{B_l^2(\mathbf{n}, z) - B_t^2(\mathbf{n}, z)} \right). \quad (6)$$

Thermal dust

For thermal dust emission and defining

$$dI_\nu^{dust}(\mathbf{n}) = \epsilon^{dust}(\nu) n_{dust}(\mathbf{n}, z) dz \quad (7)$$

we can write

$$I_\nu^{dust}(\mathbf{n}) = \int dI_\nu^{dust}, \quad (8)$$

$$Q_\nu^{dust}(\mathbf{n}) = \int dI_\nu^{dust} p^{dust} \cos(2\gamma(\mathbf{n}, z)) \cdot f_g(\mathbf{n}, z) f_{ma}(\mathbf{n}, z), \quad (9)$$

$$U_\nu^{dust}(\mathbf{n}) = \int dI_\nu^{dust} p^{dust} \sin(2\gamma(\mathbf{n}, z)) \cdot f_g(\mathbf{n}, z) f_{ma}(\mathbf{n}, z). \quad (10)$$

where ϵ^{dust} is the dust emissivity, p^{dust} is the polarization fraction, γ is the polarization angle, and, f_g and f_{ma} are polarization suppression factors (see below). Hereafter, the polarization fraction p^{dust} is set to 10% following Ponthieu et al 2005.

As discussed before, dust grains in the ISM are oblate and will align with their large axis (see Figure 3) perpendicularly to the magnetic field lines (Davis & Greenstein 1951, Lazarian 1995, Lazarian 1997, Lazarian 2009). Therefore, the polarization direction, for thermal dust emission will be perpendicular both to the magnetic field lines and the line-of-sight as was already the case for the synchrotron emission. Then, the polarization angle γ will be the same for the synchrotron and dust emission. However, as the dust grains rotate with their spin axis parallel to the magnetic field we also need to account for a geometrical suppression factor. For example, if the magnetic field direction is parallel to the line-of-sight we expect the dust polarized emission to be fully suppressed. The suppression factor can be expressed as $f_g = \sin^2(\alpha)$ where α is the angle between the

magnetic field direction and the line-of-sight. By construction, we observe that γ and α are the same angle. The process of alignment of the dust grains with the magnetic field is very complex (Mathis 1986, Goodman & Whittet 1995, Lazarian 1995, Lazarian 1997, Lazarian 2009) and its accurate representation is out of the scope of this paper. Then, to account for missalignments between the dust grains and the magnetic field lines we define an empirical factor f_{ma} . The form of this factor is unknown but we have empirically observed that the geometrical suppression seems to be more important than expected for the Archeops data. Therefore, we have taken f_{ma} to be $\propto \sin(\alpha)$. We have observed that the results presented on this paper are robust with respect to this parameter.

3.1. Matter density model

In galactocentric cylindrical coordinates (r, z, ϕ) the relativistic electron density distribution can be written as (see Drimmel & Spergel 2001)

$$n_{\text{CRE}}(r, z) = n_{0,e} \cdot \frac{e^{-\frac{r}{n_{\text{CRE},r}}}}{\cosh(z/\text{kpc}) \cosh(z/n_{\text{CRE},h})}, \quad (11)$$

where $n_{\text{CRE},h}$ defines the width of the distribution vertically and is set to 1 kpc in the following. $n_{\text{CRE},r}$ defines the distribution radially and it is a free parameter of the model. Notice that we expect these two parameters to be strongly correlated and that is why we have decided to fix one of them as was the case on previous analyses (Sun et al 2008, Jaffe et al 2009).

The density distribution of dust grains in the Galaxy is poorly known and that is why we have chosen to describe it in the same way that the relativistic electrons one

$$n_d(r, z) = n_{0,d} \cdot \frac{e^{-\frac{r}{n_{d,r}}}}{\cosh^2(z/n_{d,h})}, \quad (12)$$

where $n_{d,r}$ and $n_{d,h}$ are the radial and vertical widths of the distribution. In the following we set them to 3 and 0.1 kpc respectively.

3.2. Galactic magnetic field model

According to observations, many spiral galaxies in our vicinity and for various redshifts, present a large scale magnetic field with intensity of the order of few μG and direction spatially correlated with the spiral arms (Sofue et al 1986, Beck et al 1996, Wielebinski 2005). For our Galaxy, the magnetic field direction also seems to follow the spiral arms but with a complex spatial distribution (Wielebinski 2005, Han et al 2006, Beck 2006). Indeed, there are hints for local inversion of the field direction and radial dependency of the intensity (Han et al 2006, Beck 2001). Pulsar Faraday rotation measurements (Han et al 2004, Han et al 2006, Sofue et al 1986, Brown et al 2007) have been used to

fit the Galactic large-scale magnetic field with various models including a axi-symmetric or bi-symmetric form, a field that reverses in the inter-arm regions, etc. Pulsar Faraday rotation measurements also indicate the presence of a turbulent component of the magnetic field (Han et al 2004).

3.2.1. Large-scale magnetic field.

In the following we consider a Modified Logarithmic Spiral (MLS) model of the large-scale magnetic field based on the WMAP team model presented in Page et al (2007). It assumes a logarithmic spiral to mimic the shape of the spiral arms (Sofue et al 1986) to which we have added a vertical component. In galactocentric cylindrical coordinates (r, z, Φ) it reads

$$\begin{aligned} \mathbf{B}(\mathbf{r}) = & B_{reg}(\mathbf{r})[\cos(\phi + \beta) \ln\left(\frac{r}{r_0}\right) \sin(p) \cos(\chi) \cdot \mathbf{u}_r \\ & - \cos(\phi + \beta) \ln\left(\frac{r}{r_0}\right) \cos(p) \cos(\chi) \cdot \mathbf{u}_\phi \\ & + \sin(\chi) \cdot \mathbf{u}_z], \end{aligned} \quad (13)$$

where p is the pitch angle and $\beta = 1/\tan(p)$. r_0 is the radial scale and $\chi(r) = \chi_0(r)(z/z_0)$ is the vertical scale. Following Taylor & Cordes 1993 we restrict our model to the range $3 < r < 20$ kpc. The lower limit is setted to avoid the center of the Galaxy for which the physics is poorly constrained and the model diverges. The intensity of the regular field is fixed using pulsar Faraday rotation measurements by Han et al 2006

$$B_{reg}(r) = B_0 e^{-\frac{r-R_\odot}{R_B}} \quad (14)$$

where the large-scale field intensity at the Sun position is $B_0 = 2.1 \pm 0.3 \mu G$ and $R_B = 8.5 \pm 4.7 kpc$. The distance between the Sun and the Galactic center, R_\odot is set to 8 kpc (Eisenhauer et al 2003, Reid & Brunthaler 2005).

We also study the spiral model of Stanev 1997, Sun et al 2008, hereafter ASS. In cylindrical coordinates it is given by

$$B_r^D = D_1(r, \Phi, z) D_2(r, \Phi, z) \sin(p) \quad (15)$$

$$B_\Phi^D = -D_1(r, \Phi, z) D_2(r, \Phi, z) \cos(p) \quad (16)$$

$$B_z^D = 0 \quad (17)$$

where D_1 accounts for the spatial variations of the field and D_2 for asymmetries or reversals in the direction. The pitch angle is defined as for the MLS model described above. $D_1(r, z)$ is given by

$$D_1(r, z) = \begin{cases} B_0 \exp\left(\frac{r-R_\odot}{R_0} - \frac{|z|}{z_0}\right) & r > R_c \\ B_c & r \leq R_c \end{cases}. \quad (18)$$

where R_\odot is the distance of the Sun to the center of the Galaxy and it is set to 8 kpc as before. R_c is a critical radius and it is set to 5 kpc following the ASS+RING model in Sun et al 2008. In the same way R_0 is fixed to 10 kpc, B_0 to 6 μG and B_c to 2 μG . The field reversals are specified by

$$D_2(r) = \begin{cases} +1 & r > 7.5 \\ -1 & 6 < r \leq 7.5 \\ +1 & 5 < r \leq 6 \\ -1 & r < 5 \end{cases} \quad (19)$$

where r is defined in units of kpcs.

It is important to notice that the synchrotron and thermal dust polarized emission depends only on the orientation and not on the sign of the magnetic field and therefore, they are not sensible to field reverses in the model.

3.2.2. Turbulent component

In addition to the large-scale Galactic magnetic field, Faraday rotation measurements on pulsars in our vicinity have revealed a turbulent component for scales smaller than few hundred pc (Lyne & Smith 1989). Moreover this turbulent field seems to be present at large scales (Han et al 2004). The amplitude of this turbulent component is estimated to be of the same order of magnitude as the amplitude of the regular one (Han et al 2006). The magnetic energy $E_B(k)$ associated with the turbulent component is well described by a Kolmogorov spectrum (Han et al 2004, Han et al 2006)

$$E_B(k) = C \left(\frac{k}{k_0}\right)^\alpha \quad (20)$$

where $\alpha = -0.37$ and $C = (6.8 \pm 0.3) \cdot 10^{-13} \text{ erg cm}^{-3} \text{ kpc}$.

3.2.3. Final model

Finally the total magnetic Galactic field $B_{tot}(\mathbf{r})$ can be written as

$$B_{tot}(\mathbf{r}) = B_{reg}(\mathbf{r}) + B_{turb}(\mathbf{r}) \quad (21)$$

where $B_{reg}(\mathbf{r})$ is the regular component, either MLS or ASS, and $B_{turb}(\mathbf{r})$ is the turbulent one. We define A_{turb} as the relative intensity of the turbulent component with respect to the regular one and it is a free parameter of the model. The turbulent component is computed from a 3D random realization of the Kolmogorov spectrum

presented above over a box of 512^3 points of 56 pc resolution.

In this paper we do not consider the halo component presented by Sun et al 2008, Jansson et al 2009) as relativistic electrons and dust grains are not expected to be concentrated on the halo.

3.3. Emissivity model in polarization

As discussed in the previous section, the polarized emission in the 23 GHz WMAP data shows complex structures both on the Galactic plane and in local high Galactic latitude structures such as the North Celestial Spur (Page et al 2007). An accurate representation of this complexity can not be achieved using a simplified model like the one presented here. A similar degree of complexity is observed in the 353 GHz polarization maps although the morphology of the structures is rather different. To account for this complexity the Q and U estimate for synchrotron and thermal dust models are corrected using intensity templates of these components extrapolated to the observation frequencies (23 and 353 GHz) using constant spectral indices.

For the synchrotron emission we have

$$Q_s = I_{\text{Has}} \left(\frac{\nu}{0.408} \right)^{\beta_s} \frac{Q_\nu^{\text{sync}}}{I_\nu^{\text{sync}}}, \quad (22)$$

$$U_s = I_{\text{Has}} \left(\frac{\nu}{0.408} \right)^{\beta_s} \frac{U_\nu^{\text{sync}}}{I_\nu^{\text{sync}}}, \quad (23)$$

where I_{Has} is the reference map in intensity constructed from the 408 MHz all-sky survey (section 2.1.1) after subtraction of the free-free emission and ν is the frequency of observation. Notice that we do not use the synchrotron MEM intensity map at 23 GHz (Hinshaw et al 2007) as a synchrotron template to avoid any possible spinning dust contamination. The spectral index β_s used to extrapolate maps at various frequencies is assumed to be spatially constant on the sky and is a free parameter of the model.

For the thermal dust emission we write

$$Q_d = I_{sfd} \frac{Q_\nu^{\text{dust}}}{I_\nu^{\text{dust}}}, \quad (24)$$

$$U_d = I_{sfd} \frac{U_\nu^{\text{dust}}}{I_\nu^{\text{dust}}}, \quad (25)$$

where I_{sfd} is the reference map in intensity at 353 GHz generated using model 8 of Schlegel, Finkbeiner and Davis (Finkbeiner et al 1999) which was obtained from the IRAS Schlegel et al 1998 and COBE/DIRBE data (Boulanger et al 1996).

We compute the above I, Q and U maps for synchrotron and thermal dust with the help of a modified version of the Hammurabi code (Waelkens et al 2009). Each map is generated by integrating in 100 steps along each line-of-sight defined by the HEALPix

Table 1. Latitude and longitude bands for the Galactic profiles used in the analysis.

Latitude interval (deg)	[0, 30]	[30, 90]	[90, 120]	[120, 180]	[180, 270]	[270, 330]	[330, 360]
Longitude interval (deg)	[-90, -50]	[-50, -20]	[-20, -5]	[-5, 5]	[5, 50]	[50, 70]	[70, 90]

Table 2. Parameters of the 3D Galactic model.

Parameter	Range	Binning
p (deg)	[-80.0, 80.0]	10.0
A_{turb}	[0, 2.5] * B_{reg}	0.25
$n_{CRE,r}$ (kpc)	[0.0, 10.0]	1
β_s	[-4.3, -2.4]	0.1

$N_{side} = 128$ pixel centres. The integration continues out to 25 kpc from the observer situated 8.5 kpc from the Galactic centre.

4. Galactic-profiles comparison

4.1. Galactic-profiles description

In order to compare the models of Galactic polarized emission to the available data we compute Galactic longitude and latitude profiles for the models and for the data in temperature and polarization using the set of latitude and longitude bands defined in Table 1. For the Galactic longitude and latitude profiles both, we use bins of longitude of 2.5° . In the following discussions we will only consider Galactic latitude profiles because equivalent results are obtained with the longitudinal profiles.

We compute error bars including intrinsic instrumental uncertainties and the extra variance induced by the presence of a turbulent component. The latter is estimated from the RMS within each of the latitude bins following Jansson et al 2009. For the 408 MHz all-sky survey we account for intrinsic uncertainties due to the 10 % calibration errors described in Section 2. For the WMAP 23 GHz data we have computed 600 realizations of Gaussian noise maps from the number of hits per pixel and the sensitivity per hit given on the WMAP LAMBDA web site. We have computed Galactic latitude profiles in polarization for these simulated maps and estimated intrinsic errors from the standard deviation within each latitude bin. For the Archeops data we use the noise simulations discussed in Macías-Pérez et al 2007 and proceed as for the WMAP data.

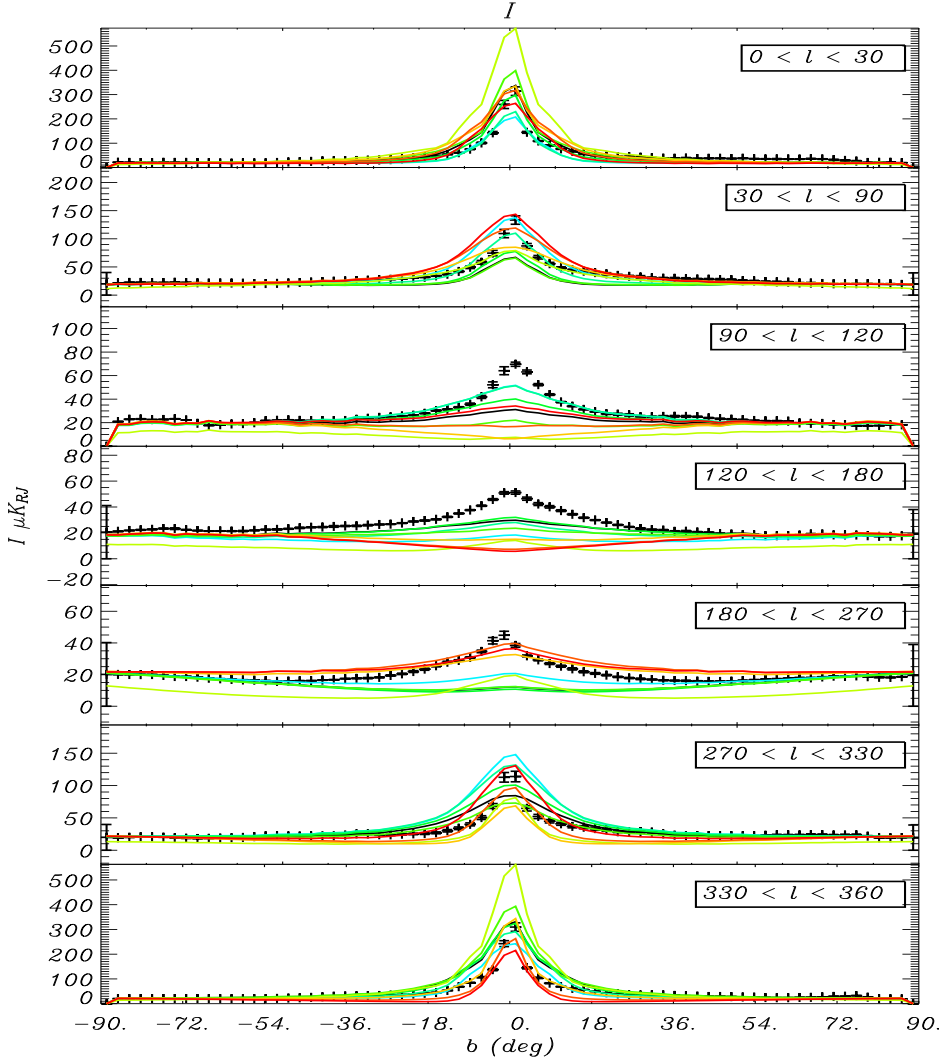


Fig. 4. Galactic profiles in temperature at 408 MHz built using the Haslam data (*black*) and the model of synchrotron emission with MLS for various values of the pitch angle p (*from green to red*).

Galactic latitude profiles are computed for a grid of models obtained by varying the pitch angle, p , the turbulent component amplitude, A_{turb} , the radial scale for the synchrotron emission, $n_{CRE,r}$ and the synchrotron spectral index, β_s . The range and binning step considered for each of these parameters is given in Table 2. All the other parameters of the model of the Galactic magnetic field and matter density are fixed to values proposed in Section 3. Notice that to be able to compare the dust models to the Archeops 353 GHz data, the simulated maps are multiplied by a mask accounting for the Archeops incomplete sky coverage.

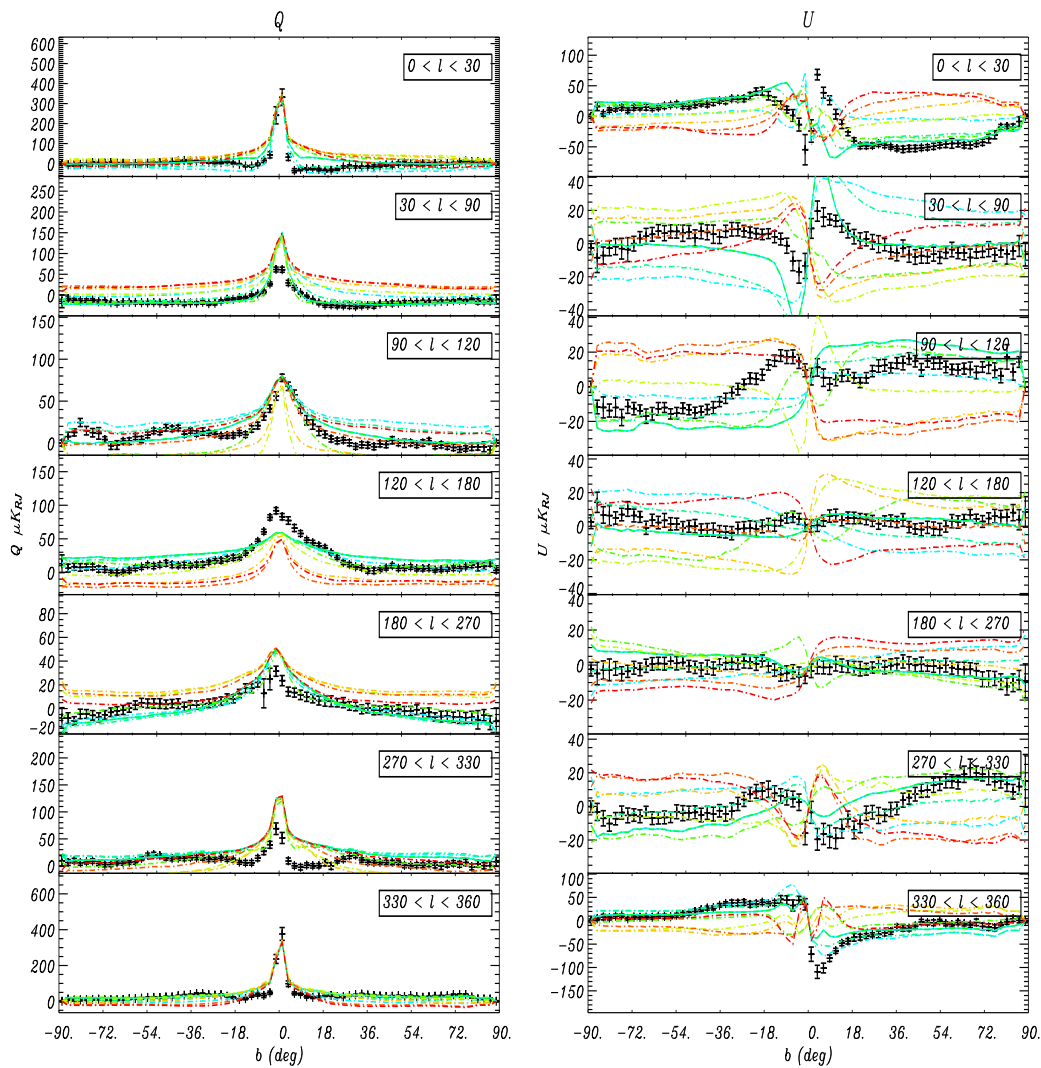


Fig. 5. Galactic profiles in polarization Q and U at 23 GHz built with the five-year WMAP data (*black*) and the model of synchrotron emission with MLS magnetic field for various values of the pitch angle p (*form green to red*).

Figure 4 shows in black Galactic latitude profiles in temperature for the 408 MHz all-sky survey with error bars computed as discussed above. In colors, we show for comparison the expected synchrotron diffuse Galactic emission from the MLS Galactic magnetic field model for various values of the pitch angle p . On Figure 5 we present the polarization Galactic latitude profiles for the WMAP 23 GHz data (black) and the expected polarized diffuse synchrotron emission for the previous MLS models (color). Finally, Figure 6 shows the polarization Galactic latitude profiles for the 353 GHz Archeops data (black) compared to the same MLS models (color). From these figures we can see that the current available data do help discriminating between the different models and therefore a likelihood analysis is justified.

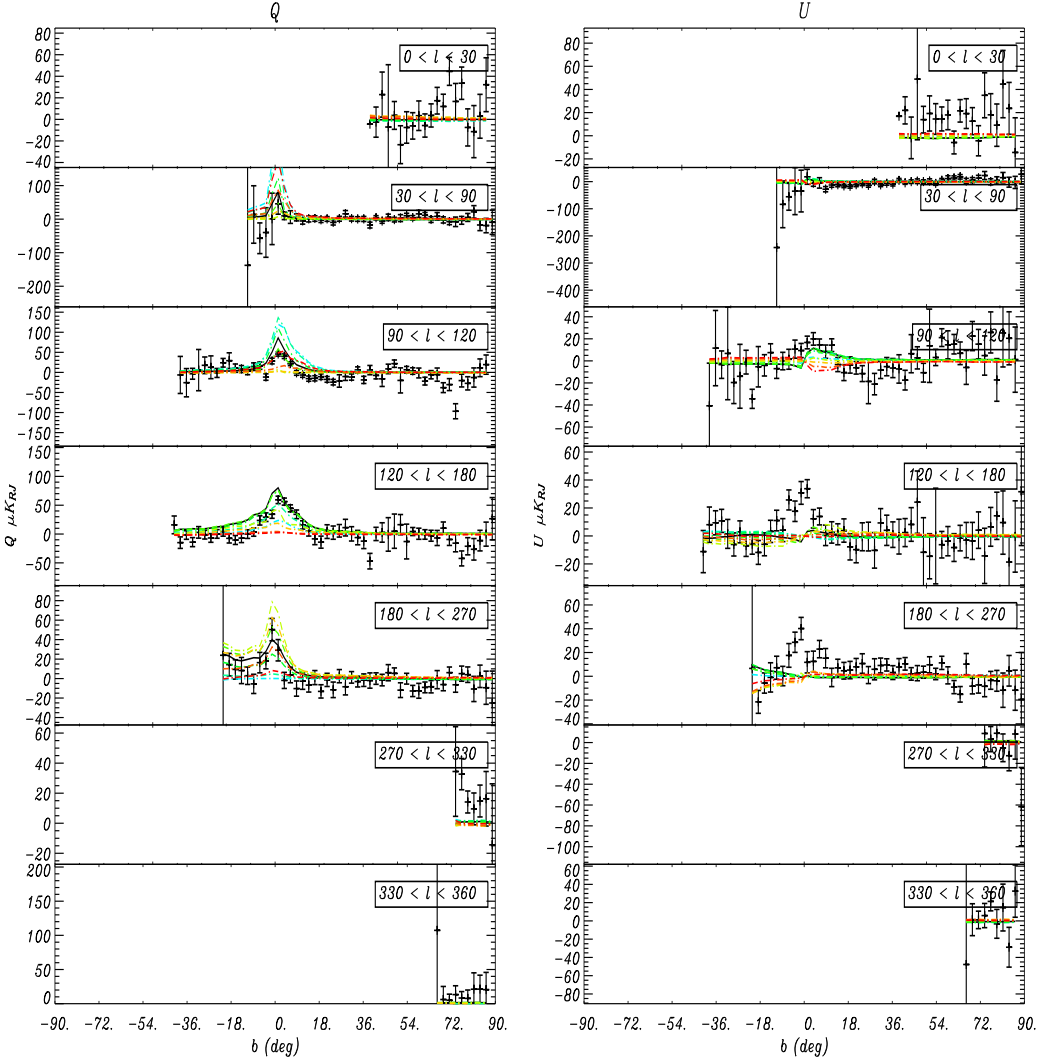


Fig. 6. Galactic profiles in temperature and polarization Q and U at 353 GHz with the ARCHEOPS data (*black*) and for various values of the pitch angle p for the model in polarization of thermal dust emission with MLS magnetic field (*from green to red*).

4.2. Likelihood analysis

The data and model Galactic latitude profiles are compared using a likelihood analysis where the total likelihood function is obtained from

$$\mathcal{L}_{tot} = \prod_{d=1}^3 \mathcal{L}_d \quad (26)$$

where for each of the 3 data sets described above the log-likelihood function is given by

$$-\log \mathcal{L}_d = \sum_i \sum_{j=0}^{N_{lon}-1} \sum_{k=0}^{N_{lat}-1} \frac{(D_{i,j,k}^d - M_{i,j,k}^d)^2}{\sigma_{i,j,k}^d} \quad (27)$$

where i represents the polarization state meaning intensity only for the 408 MHz all-sky survey, and, Q and U polarization for the 23 GHz WMAP and 353 GHz

Table 3. Best-fit parameters for the MLS and ASS models of the Galactic magnetic field.

Data	Magnetic field model	$p(deg)$	A_{turb}	$n_{CRE,r}$	β_s	χ^2_{min}
408 MHz	MLS	$-20.0^{+60.0}_{-50.0}$	< 1.00 (95.4 % CL)	4^{+16}_{-3}	\emptyset	3.58
	ASS	$-10.0^{+80.0}_{-70.0}$	< 1.0 (95.4 % CL)	5^{+15}_{-3}	\emptyset	4.65
WMAP 23 GHz	MLS	$-30.0^{+40.0}_{-30.0}$	< 1.25 (95.4 % CL)	< 20 (95.4 % CL)	$-3.4^{+0.1}_{-0.8}$	5.72
	ASS	$-40.0^{+60.0}_{-30.0}$	< 1.5 (95.4 % CL)	3^{+17}_{-2} (95.4% CL)	$-3.4^{+0.1}_{-0.8}$	7.62
Archeops 353 GHz	MLS	-20^{+80}_{-50}	< 2.25 (95.4%CL)	\emptyset	\emptyset	1.98
	ASS	60.0^{+20}_{-40}	$0.25^{+2.0}_{-0.25}$	\emptyset	\emptyset	1.72
All	MLS	-20^{+80}_{-50}	< 2.25 (95.4%CL)	\emptyset	\emptyset	1.98
	ASS	60.0^{+20}_{-40}	$0.25^{+2.0}_{-0.25}$	\emptyset	\emptyset	1.72

Archeops data. j and k represents the longitude bands and latitude bins respectively.

$D_{i,j,k}^d$ and $M_{i,j,k}^d$ corresponds to the data set d and model for the i polarization state, j longitude band and k latitude bin, respectively. $\sigma_{i,j,k}^d$ is the error bar associated to $M_{i,j,k}^d$.

Table 3 presents the best-fit parameters for the three-data sets described above and also for the combination of three of them (labeled All in the table). Results are presented both for the MLS and ASS models of the Galactic magnetic field. The best-fit value for the pitch angle, p , are in agreement within $1-\sigma$ error bars for the three data sets but for the Archeops data in the case of an ASS model. Notice that our results are compatible with the pitch angle values presented in Sun et al 2008, Page et al 2007, Miville-Deschênes et al 2008. The relative amplitude of the turbulent component, A_{turb} , is poorly constrained and the data does not seem to favour a strong turbulent component either in the case of MLS or ASS models. However, our results are compatible with the ones presented in Sun et al 2008, Miville-Deschênes et al 2008, Han et al 2004, Han et al 2006 at the $2-\sigma$ level. The electronic density radial scale, $n_{CRE,r}$, is poorly constrained by the data both for MLS and ASS models although our results are compatible with those of Sun et al 2008. We also tested the possibility of a local contribution to the electronic density as proposed by Sun et al 2008. We found that adding this local component does not improve either the fit or the constraint on the radial scale. The best-fit value for the spectral index of the synchrotron emission seems to be significantly lower than the one in Sun et al 2008, Page et al 2007. This may due to differences in the intensity template. Notice that we rescale the polarization intensity using the 408 MHz all-sky survey to obtain a more realistic model.

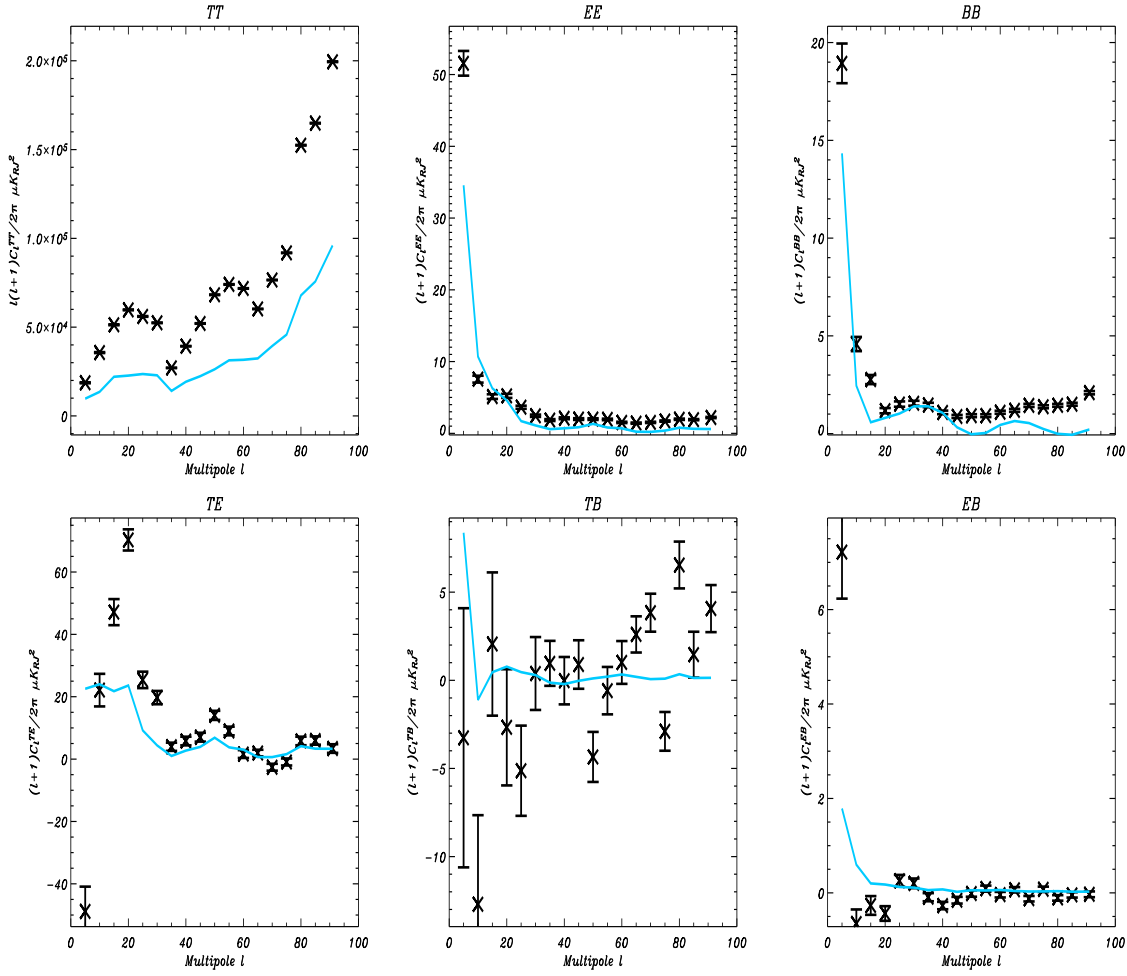


Fig. 7. From left to right and from top to bottom : power spectra $C_l^{TT}, C_l^{EE}, C_l^{BB}, C_l^{TE}, C_l^{TB}, C_l^{EB}$ at 23 GHz built with the WMAP 5-year data (black) and the model of synchrotron emission with MLS magnetic field for the best fit model parameters, excluding the Galactic region defined by $|b| < 5^\circ$.

4.3. Temperature and polarization angular power spectra

Using the best-fit parameters of the MLS model, $p = -30.0^\circ$, $A_{turb} = 0.0$, $n_{CRE,r} = 1$ and $\beta_s = -3.4$, we have constructed simulated maps of the sky at 408 MHz and 23 and 353 GHz. These maps are shown on right-hand side of Figures 2.1.1 and 2. Although for the Galactic profiles the fit can be considered relatively good, the fake temperature map at 408 MHz looks very different from the 408 MHz all-sky survey map (left side of the plot), in particular at the North Polar Spur (Wolleben et al 2007), as no local structures were included in the model. This supports a posteriori our correction of the polarization synchrotron model using an intensity template as presented in Section 3. In Q and U polarization, the 23 GHz fake maps seem to reproduce qualitatively the structure observed in the WMAP data (left side of the plot). However in temperature the model and the data are very different as we have not account for a variable synchrotron

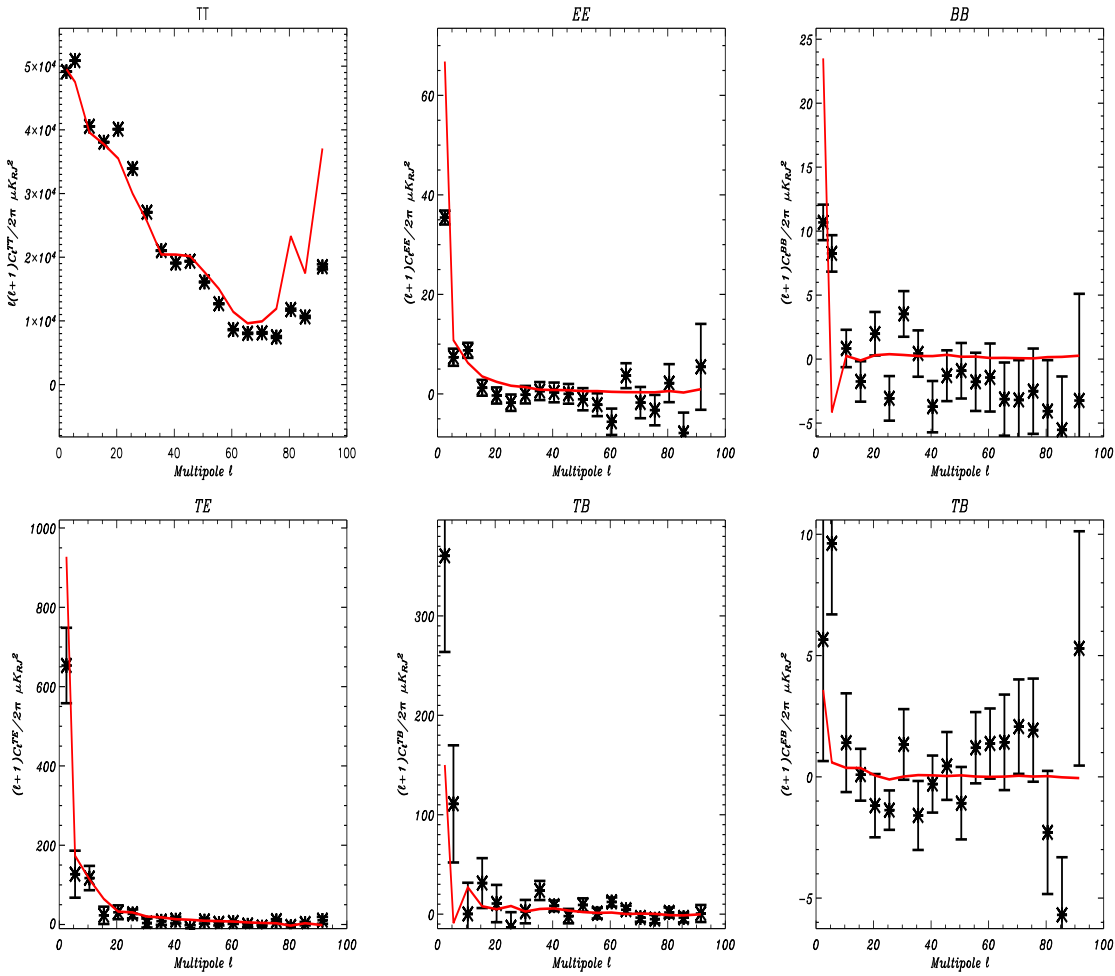


Fig. 8. From left to right and from top to bottom: power spectra $C_l^{TT}, C_l^{EE}, C_l^{BB}, C_l^{TE}, C_l^{TB}, C_l^{EB}$ at 353 GHz computed from ARCHEOPS data (black) and the model of thermal dust emission with MLS magnetic field for the best fit model parameters (red) for the full-sky.

spectral nor for any extra component as discussed in Page et al 2007, Kogut et al 2007, Miville-Deschênes et al 2008, Macías-Pérez et al 2010. Finally, the model of thermal dust emission is able to reproduce qualitatively the Archeops data at 353 GHz.

Figures 7 and 8 show the temperature and polarization angular power spectra for the 23 GHz WMAP and 353 GHz Archeops data compared to the best-fit MLS model for synchrotron and dust, respectively. As discussed before, the temperature auto power spectrum of the 23 GHz data is very different from the model as no extra components in temperature were considered. However in polarization we have qualitatively a good agreement. However, we clearly observe that the model does not account for all the observed emission. At 353 GHz the agreement between the data and the model qualitatively and quantitatively is good. For polarization most of the data

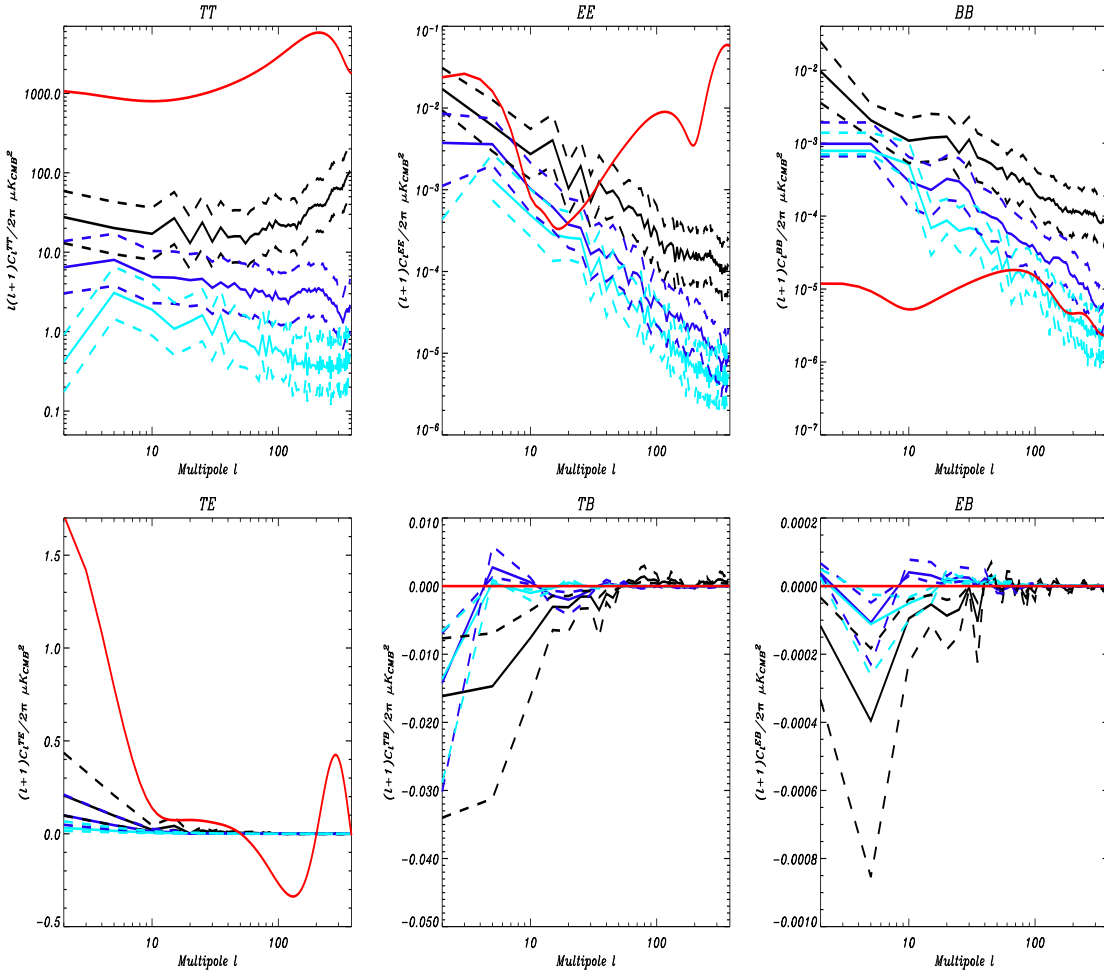


Fig. 9. From left to right and from top to bottom: power spectra $C_l^{TT}, C_l^{EE}, C_l^{BB}, C_l^{TE}, C_l^{TB}, C_l^{EB}$ at 100 GHz the model of Galactic polarized emission applying a Galactic cut of $|b| < 15^\circ$ (black) 30° (blue) and 40° (cyan) and compared them to the expected CMB ones (red) for the WMAP best-fit Λ CDM model (Komatsu et al 2008) to which we added a tensor component assuming an tensor to scalar ratio of 0.1..

samples at less than $3\text{-}\sigma$ from the model. In temperature the model is not as accurate as in polarization but we notice that the fitting was restricted to polarization data only.

5. Galactic foreground contamination to the CMB measurements by the Planck satellite

We can use the best-fit model of polarized synchrotron and dust emission to estimate the polarized foreground contamination to the CMB at the Planck satellite observation frequencies. We are interested in comparing the expected foreground contribution to the expected CMB emission. Notice that the aim of this section is not to obtain an accurate template of the polarized Galactic foreground emission to be subtracted on the Planck

data for CMB purposes.

For this purpose, we have produced simulated maps of the Galactic polarized foreground emission using the best-fit model parameters for each of the Planck CMB frequencies, 70, 100, 143 and 217 GHz. The thermal dust polarized emission have been extrapolated using a constant spectral index of 2.0 in antenna temperature. We have computed the temperature and polarization power spectra of these maps and compared them to the expected CMB ones for the WMAP best-fit Λ CDM model (available on the LAMBDA website) to which we added a tensor component assuming a tensor to scalar ratio of 0.1. Note that neither noise nor systematics nor resolution effects are considered.

Figure 9 shows these power spectra at 100 GHz. The expected CMB signal is represented in red. The polarized diffuse foreground emission for Galactic latitude cuts of $|b| < 15^\circ$, 30° and 40° are shown in solid black, blue and cyan lines, respectively. $1-\sigma$ errors in the model are represented by dashed lines. In temperature, the CMB C_l^{TT} dominates at all the angular scales considered as could be expected from the WMAP and Archeops data. For polarization, the CMB C_l^{EE} dominates at high ℓ values but we observe significant foreground contamination at the lowest ℓ values ($\ell < 20$). In the same way, the CMB C_l^{TE} dominates at 100 GHz but for very low ℓ values. However, the CMB C_l^{BB} is significantly smaller than the foreground contribution at all the angular scales considered even for such a large value of the tensor to scalar ratio. The CMB C_l^{TB} and C_l^{EB} are expected for most cosmological models to be null and therefore, the foreground contribution dominates the signal.

As the Galactic polarized foreground emission seems to dominate the observed emission at the Planck CMB frequencies, special care should be taken when estimating the CMB emission using standard template subtraction techniques and component separation algorithms. The assessment of the final errors is crucial and we think that models of the polarized foreground emission such as those presented in this paper can be of much help for this task.

6. Summary and conclusions

We have presented in this paper a detailed study of the diffuse synchrotron and thermal dust polarized Galactic foreground emission components. We have constructed coherent models of these two foregrounds based on a 3D representation of the Galactic magnetic field and of the distribution of relativistic electrons and dust grains in the Galaxy. For the Galactic magnetic field we have assumed a large-scale regular component plus a turbulent one. The relativistic electron distribution and dust grain distribution have been modeled as exponentials peaking at the Galactic center. From these analyses we have been able to study the main parameters of the models, the magnetic field pitch angle, p , the radial

width of the relativistic electron distribution, h_{er} , the relative amplitude of the turbulent component, A_{turb} and spectral index of the synchrotron emission β_s . We have been able to set constraints only on the pitch angle and the synchrotron spectral index. An upper limit on the relative amplitude of the turbulent component is obtained although the data seems to prefer no turbulence at large angular scales. With the current data we are not able to constrain the radial width of the relativistic electron distribution. Notice that our constraints are compatible with those in the literature.

Using the best-fit parameters we have constructed maps in temperature and polarization for the synchrotron and dust thermal emission at 23 and 353 GHz and compare them to the WMAP and ARCHEOPS data at the same frequencies. We find good agreement between the data and the model. However, when comparing the temperature and polarization power spectra for the data and model maps, we observe that synchrotron emission model is not realistic enough. For dust the model seems to reproduce better the data but it is important to realize that the errors on the Archeops data are much larger.

From this, we can conclude that the models presented in this paper can not be used for direct subtraction of polarized foregrounds for CMB purposes. However they can be of great help for estimating the impact of the polarized Galactic foreground emission on the reconstruction of the CMB polarized power spectra. Indeed, we have extrapolated the expected polarized Galactic foreground emission to the Planck CMB frequencies, 70, 100, 143 and 217 GHz and found they dominate the emission at low ℓ values where the signature in the polarized CMB power spectra of important physical processes like reionization is expected. Furthermore, the Galactic polarized foreground emission seems to dominate the B modes for which we expect an unique signature from primordial gravitational waves. Because of this, we propose the use of models like the ones presented in this paper to asses the errors in the reconstruction of the CMB emission when using template subtraction techniques or component separation algorithms.

References

- Battistelli, E.S. et al, 2006, ApJ, **645**, 141-144
Baumann D. et al, 2009, AIP Conf.Proc., **1141**.
Beck R. et al, 1996, ARA&A, **34**, 155.
Beck R., Space Science Reviews, **99**, 243.
Beck R., 2006, *Proceedings of Polarization 2005*, EAS Publication Series
Benoît et al, 2004, A & A, **424**, 571.
Betoule et al, 2009, A & A, **503**, 691B.
Boulanger F. et al, 1996, A&A, **312**, 181.
The Planck Consortia, *The Scientific Program*, 2004.
Brouw N.W. & Spoelstra T.A.T., 1976, A.& A. Sup. S., **26**, 129.
Brown J.C. et al., 2007, ApJ, **663**, 258-266.
Burn B. J. et al 1966, MNRAS, **133**, 67B.

- Carretti E. et al 2009, **astro-ph/0907.4861v1**
- Cordes J.M. & Lazio T.J.W., 2002, **astro-ph/0207156**.
- Davis B. T. & Greenstein J. L., 1951, ApJ, **114**, 206.
- Desert F.-X. et al, 1998, A&A, **342**, 363.
- Desert F.-X. et al, 2008, A&A, **481**, 411D.
- Dickinson C., Davies R. D. & Davis R. J., 2003, MNRAS, **341**, 369.
- Drimmel R. & Spergel D.N., 2001, ApJ, **556**, 181.
- Duncan A. et al, 1999, A. & A., **350**, 447.
- Eisenhauer F. et al, 2003, ApJ, **597**, L121.
- Efstathiou G. et al, 2009, MNRAS, **397**, 1355.
- Efstathiou G & Gratton S., 2009, JCAP,**6**, 11.
- Finkbeiner D. P., Davis M. & Schlegel D. J., 1999, ApJ, **524**, 867 .
- Gold B. et al, 2009, ApJS, **180**, 265.
- Goodman A. A. & Whittet D. C. B., 1995, ApJ, **455**, 181.
- Górski K.M. et al, 2005, ApJ, **622**,759.
- Hall J.S.,1949, Science, **109**, 106.
- Han J. L., Ferrière K. & Manchester R. N., 2004, A&A, **610**, 820-826.
- Han J. L. et al, 2006, A&A, **642**, 868.
- Haslam C.G.T.et al, 1982, A&AS, **47**, 1.
- Heiles C.,2000, ApJ, **119**, 923.
- Hildebrand R. H. et al, 1999, ApJ, **516**, 834.
- Hiltner W.A., 1949, Science, **109**, 65.
- Hinshaw G. et al, 2007, ApJS, **170**, 288.
- Jaffe T. et al, 2009, MNRAS,**401**, 1013.
- Jansson R. et al, 2009, JCAP, **7**, 21.
- Kogut A. et al, 2007, ApJ, **665**, 355.
- Komatsu E. et al, 2008, ApJS, **180**, 306.
- Lazarian A., 1995, MNRAS, **277**, 1235-1242.
- Lazarian A. et al, 1997, ApJ, **490**, 273.
- Lazarian A. et al, 2009, ASP Conference Series, **4**.
- Leach S. M. et al, 2008, A&A, **491**, 597.
- Lyne A.G. & Smith F.G., 1989, MNRAS, **237**, 533.
- Mathis J. S., 1986, ApJ, **308**, 281.
- Macías-Pérez J. F., Lagache G., Maffei F. et al., 2007, A&A, **467** 1313.
- Macías-Pérez J. F.,Desert F.-X., Tristram M., Fauvet L. et al in preparation.
- Miville-Deschênes M. -A. et al, 2008, A&A, **490**, 1093.
- Nolta M.R., 2009, ApJS, **180**, 296.
- Page L. et al, 2003, ApJS, **148**, 39.
- Page L. et al, 2007, ApJSS, **170**, 335.
- Peiris H. et al, 2003, ApJS, **148**, 213.
- Ponthieu N., Macías-Pérez J. F, Tristram M. et al, 2005, A&A, **444**, 327.

- Reid M. & Brunthaler A., 2005, in ASP Conf. Ser. 340, Future Directions in High Resolution Astronomy: The 10th Anniversary of the VLBA, ed. J. Romney & M. Reid (San Francisco: ASP), 253 .
- Ribicki G.B. & Lightman A., 1979, Radiative Process in Astrophysics (New York, Wiley-Interscience).
- Schlegel D. J., Finkbeiner D.P. & Davis M., 1998, ApJ, **500**, 525.
- Sofue Y., Fujimoto M. & Wielebinski R., 1986, ARA&A, **24**, 459.
- Stanev T., 1997, ApJ, **479**, 290.
- Sun X.H., Reich W., Waelkens A. & Ensslin T.A., 2008, A&A, **477**, 573.
- Taylor J. H. J. & Cordes J. M., 1993, ApJ, **411**, 674.
- Uyaniker B. et al, 1999, A&AS, **132**, 401.
- Vaillancourt J. E., 2002, ApJS, **142**, 335.
- Waelkens A., Jaffe T. et al, 2009 A&A, **495**, 697.
- Wielebinski R., 2005, *Cosmic Magnetic Field*, ed. R. W. R. reck, Springer, Berlin.
- Wolleben M. et al, 2006, A.& A., **448**, 411.
- Wolleben M. et al, 2007, ApJ, **664**, 349.